Effects of K-dopant on structure and activity of KMn/Al_2O_3 catalysts for CO oxidation: experimental evidence and DFT calculation

Xiaopei Xie[a], QinghuTang[a]*, Jia Zhang[b]*, Jing Wang[a], Peizheng Zhao[a], Yi Wang[c], Michael B. Sullivan[b], Yanhui Yang[d]

[a] School of Chemistry and Chemical Engineering, Key Laboratory of Green Chemical Media and Reactions, Ministry of Education, Henan normal University, Xinxiang 453007, P.R. China

[b] Institute of High Performance Computing, Agency for Science, Technology and Research, Singapore 138632

[c] National Engineering Laboratory for Hydrometallurgical Cleaner Production Technology, Institute of Process Engineering, Chinese Academy of Sciences, Beijing 100190, P.R. China

[d] School of Chemical and Biomedical Engineering, Nanyang Technological University,Singapore 637459, Singapore

* To whom correspondence should be addressed.

Email address: qinghutang@sina.com.cn & zhangj@ihpc.a-star.edu.sg

Abstract

KMn/Al_2O_3 catalysts with different K:Mn molar ratios were synthesized by a facile impregnation method and attempted for CO oxidation. The correlation in between potassium-dopant amount and the structure/ catalytic activity of KMn/Al_2O_3 catalysts were investigated. Doping small amount of potassium (K:Mn mole ratio less than 1:10) to Mn/Al_2O_3 catalyst efficiently enhanced the catalytic activity of Mn/Al_2O_3 catalyst. We found that the K_1Mn_{10}/Al_2O_3 catalyst exhibited the best CO oxidation activity with the TOF of 1.5×10^{-3} s^{-1} for 100% CO conversion at 260 ºC, which is 50 ºC lower than that on Mn/Al_2O_3 catalyst. However, excessive amounts of potassium led to β-to-α-MnO_2 phase transformation and poor catalytic performance. DFT calculations combined with multiple characterization techniques were performed to provide a deep insight into the K-doping effect. The results suggested that the addition of an appropriate amount of potassium to Mn/Al_2O_3 catalyst improved the dispersion of manganese oxide, the mobility and reactivity of surface lattice oxygen, thus significantly improved the catalyst activity.

Keywords: CO oxidation, manganese oxide, potassium, phase transformation

Introduction

The catalytic oxidation of CO has been identified as an important reaction because of its wide applications in indoor air quality, gas sensors, CO_2 lasers, and automobile exhaust treatment [1, 2]. Although many studies have been devoted to the catalytic oxidation of CO using noble-metal catalysts such as Au/TiO_2, Au/ZrO_2 and Pt/SnO_2 [3-5], it is still greatly desired to explore the use of less-expensive metal oxide catalysts with high activity and

stability. In particular, manganese oxides attracted attention not only because of their low-cost and environmentally friendly nature, but also their physical and chemical characteristics [6]. Manganese can exist in more than five stable and easily transformed oxidation states with multiple structural forms over a wide range of temperatures. Manganese oxides have been reported in several catalytic applications due to their highly efficient redox properties [7], and the catalytic performances can be more effective in the presence of other elemental dopants [8-11]. The improved catalytic activity observed in these modified manganese oxide catalysts was associated to the structure of the active component and the high mobility and availability of lattice oxygen [9, 12].

The positive effect of alkali metal doping has been observed in various heterogeneous catalysts [13-19]. It was reported that alkali-metal was able to enhance CO oxidation rate and decreased light-off temperatures for PdO/SnO_2[16]. Wang et al. found that the electron transfer between the Na^+ species and Pt nanoparticles played an important role in enhancing the CO-PROX performance for Na^+-intercalated carbon nanotubes-supported platinum nanoparticles [17]. Very recently, the addition of alkaline earth metal oxide was reported to promote CO oxidation over Au nanoparticles supported by TiO_2 [19]. Apart from CO oxidation reaction, alkali-metal doping effects were also explored for other important chemical reactions. For instance, Pasha and co-workers [13] reported that adding Cs led to the change in the electronic properties of NiO and thus enhanced the catalytic activity in the direct decomposition of N_2O. Doping basic promoters, e.g., alkali metal oxide or hydroxide, to a Ru/MgO catalyst afforded a significantly improved catalytic activity for ammonia synthesis [14]. In addition, a reaction pathway change, from allylic oxidation to epoxidation, was revealed in the oxidation of propylene with N_2O over Fe-MFI and Fe-MCM-41 catalysts modified by K^+ [15].

Previously, the remarkably improved catalytic activity of benzyl alcohol oxidation was

observed when modifying the Mn/AC catalyst with potassium ions [20]. The role of adding potassium has been evidenced to induce a large distortion of the Mn octahedral coordination with coexistence of Mn^{2+} and Mn^{3+}. In this work, KMn/Al_2O_3 catalysts with different K:Mn molar ratios were prepared and the catalytic activities were studied in CO oxidation. We provide experimental evidence that K doping induces a structural phase transformation and there is a correlation among doping amount– manganese oxide phases– catalytic performance. To provide insight into the K-doping effect, DFT calculations as well as multiple analytical and characterization techniques were used to investigate the structure, active sites and the reactivity of the MnO_2 catalyst surface.

Experimental

The γ-Al_2O_3 support with surface area of 193 $m^2 \cdot g^{-1}$ was prepared by precipitating $Al(NO_3)_3 \cdot 9H_2O$ with $NH_3 \cdot H_2O$ at pH of 9.0, followed by calcining at 500 ^oC for 3 h in air. KMn/Al_2O_3 catalysts with a theoretical manganese loading of 10.0 wt% were prepared by an incipient wetness method. Typically, a calculated amount of potassium nitrate (Sigma-Aldrich, 99.0%) and manganese nitrate (Fluka, $\geqslant$97.0%) was dissolved in 20 mL distilled water and mixed with 1.0 g of γ-Al_2O_3 support. The excess water was slowly evaporated in a water bath under continuous stirring. The residues were further dried overnight in a vacuum oven at 100 ^oC and then calcined at 500 ^oC for 3 h in air. The actual manganese loading in each sample was measured by inductively coupled plasma-mass spectrometry (ICP-MS) and the results were listed in Table 3.

Powder XRD patterns were collected on a Bruker Advance 8 X-ray diffractometer equipped with a rotating anode using Cu Kα radiation (λ= 0.154 nm) at a beam voltage of 40 kV and a 40 mA of beam current. N_2 physisorption isotherms were measured at -196 ^oC using a Micromeritics ASAP 2020 system. Prior to the measurement, the sample was degassed at 300 ^oC under vacuum. The specific surface area was calculated by Brunauer-Emmett-Teller

(BET) method. The XPS measurement was carried out on a PHI Quantera II Scanning ESCA Microprobe equipment (Physical Electronics) using Al-Kα radiation. The binding energy was calibrated using a C1s photoelectron peak at 284.6 eV as a reference. The surface composition was determined through the peak areas and the sensitive factors presented by Physical Electronics.

The O_2-TPD measurements were carried out with a fixed-bed quartz tubular reactor equipped with a quadrupole mass spectrometer (Omnistar, Balzers). The sample (200 mg) was loaded and heated to 300 ^oC in the He flow (30 mL $\cdot min^{-1}$) and kept at this temperature for 30 min. After cooling to room temperature, the O_2 flow (30 mL $\cdot min^{-1}$) was passed through the sample for 30 min and then the sample was purged with He (30 mL $\cdot min^{-1}$) for 1 h. After that, the reactor was heated to 900 ^oC with a ramp of 10 $^oC \cdot min^{-1}$ in the He flow (30 mL $\cdot min^{-1}$). The desorbed O_2 was monitored by the mass spectrometer.

The reducibility of Mn species supported on alumina was investigated by H_2-TPR using the flow system equipped with a thermal conductivity detector (TCD). Prior to each H_2-TPR run, 100 mg of sample was purged by ultra-zero grade air at 500 ^oC for 1 h and cooled down to room temperature. The gas flow was switched to 5 vol.% hydrogen in argon balance (30 mL $\cdot min^{-1}$), and the base line was monitored until stable. After baseline stabilization, the sample cell was heated at 10 $^oC \cdot min^{-1}$ ramping rate to 800 ^oC.

The CO oxidation activity was measured in a quartz tubular (inner diameter 9 mm) fixed-bed reactor under atmospheric pressure. The catalyst (100 mg) was loaded in the reactor. The reaction temperature was monitored by a thermocouple placed in the middle of the catalyst bed. A reaction gas consisting of 1 vol.% CO and 99 vol.% air was fed at a rate of 40 mL $\cdot min^{-1}$, corresponding to a space velocity of 24000 mL $\cdot g_{cat}^{-1} \cdot h^{-1}$. The CO and CO_2 were converted into methane and analyzed by an online GC (OuhuaGC9160) equipped with an FID detector.

Computational details

DFT calculations were performed using the Vienna Ab Initio Simulation Package (VASP) [21, 22] in which a plane-wave basis set is used. The electron-ion interaction was modelled by the projector-augmented wave (PAW) method [23, 24]. The spin-polarized GGA (generalized-gradient approximation) scheme with the Perdew-Burke-Enzerhoff (PBE) form was used for the exchange and correlation functional [25]. The plane-wave cutoff energy was set to 400 eV. The rotationally invariant DFT+U method was applied to treat the on-site coulomb interaction of d electrons in Mn ions [26]. Here, the effective U-J value was set to 4.5 eV, which has been validated from previous work to study manganese oxide surfaces [27].

As the structural phase transformation can be observed in the experiment, both α-MnO_2 and β-MnO_2 were considered in our calculations. Antiferromagnetic order was adopted for the bulk structures [28]. 3x3x9 and 6x6x9 k-point mesh with Monkhorst-Pack scheme were used for α-MnO_2 and β-MnO_2, respectively. The calculated lattice parameters are in good agreement with the experimental values (see Table1) [29, 30].

The(1x3) α-MnO_2 (100) surface and the (2x3) β-MnO_2 (110) surface were selected to study surface adsorption and reactions as they have the lowest surface energy in α-MnO_2 and β-MnO_2, respectively [31, 32]. Oxide surfaces were simulated using a slab super cell approach with periodic boundary conditions. All surface calculations were performed in a ferromagnetic configuration. As shown in Figure 1 (a), the β-MnO_2 (110) surface was modeled using a symmetric slab with three Mn-O layers and six O layers with the bottom three layers frozen. As shown in Figure 1 (c), the two units of Mn-O form a ring. The α-MnO_2 (100) slab contains three units of Mn-O and the bottom unit was fixed. On the

β-MnO_2 (110) surface, there are two types of surface O sites, including bridge O (O_{br}) and in-plane O (O_{IP}), and two types of surface Mn sites, including Mn_{5c} (Mn is in five-fold coordination) and Mn_{6c} (Mnis in six-fold coordination). Analogously, on α-MnO_2 (100) surface, we can find bridge O (O_{br}), three types of in-plane O (O_{IP1}, O_{IP2}, O_{IP3}), Mn_{5c} and Mn_{6c}. In this work, a vacuum region of 10 Å was used. 3x3x1 and 3x2x1 k-point mesh with Monkhorst-Pack scheme were adopted for α-MnO_2 (100) and β-MnO_2 (110) surface calculations, respectively. All transition states (TSs) were located using constrained minimization techniques [33].

In this work, we studied the adsorption behavior of K atom and reactant molecules on MnO_2 surfaces. The adsorption energy is defined as $E_{ad} = E_{slab+A} - E_{slab} - E_A$, where E_{slab+A} is the total energy of the slab with adsorbate, E_{slab} is the energy of the α-MnO_2 (100) or the β-MnO_2 (110) surface, and E_A stands for the energy of isolated adsorbate. By definition, a negative value corresponds to exothermic adsorption. In addition, in order to determine the most stable O vacancy, we calculated the relative energy of removing one lattice O from MnO_2 surface, where the total energy of the defect surface with an O_{IP} vacancy is set as a reference. As shown in Table 2, O_{br} is easiest to remove whether on the β-MnO_2 (110) surface or on the α-MnO_2 (100) surface.

Results and discussions

Figure 2 presents the conversions of CO over different alkali metal-doped Mn catalysts. The catalytic activity for the complete oxidation of CO follows the sequence: $CaMn/Al_2O_3$< $MgMn/Al_2O_3$, $LiMn/Al_2O_3$ < $NaMn/Al_2O_3$ < Mn/Al_2O_3 < KMn/Al_2O_3. This trend in catalytic activity can be related with the size and charge of the ions in manganese oxide (higher ratio resulted in higher activity). The characterizations of XRD and H_2-TPR (see Figure S1 and S2) showed that doping potassium to Mn/Al_2O_3 catalyst can obviously improve the dispersion

and reducibility of Mn species on the surface of the catalyst. These observed results suggest that K is a better promoter in this particular reaction. The effects of K:Mn molar ratio on the catalytic activity for CO oxidation were shown in Figure 3 and S3. Doping potassium ions significantly affected the catalytic activity of Mn/Al_2O_3 catalyst. The CO conversion over KMn/Al_2O_3 catalyst initially increased by adding potassium dopant, and subsequently declined with further increasing the K:Mn molar ratio. The K_1Mn_{10}/Al_2O_3 catalyst exhibited the best CO oxidation activity with TOF of 1.5×10^{-3} s^{-1} (100% of CO converted into CO_2) at 260 ^oC, which was 50 ^oC lower than that the required temperature for 100% CO conversion using Mn/Al_2O_3 catalyst.

The BET surface areas of KMn/Al_2O_3 samples were shown in Table 3. Compared with alumina support, the surface area of Mn/Al_2O_3 sample slightly decreased. Deposit of small manganese oxide particles on the walls and/or in the mouth of the pores of alumina may account for the decrease. The BET surface areas of KMn/Al_2O_3 samples were similar to that of the Mn/Al_2O_3 sample. Therefore, doping potassium had no significant influence on the surface area of the catalyst.

Figure 4 showed the XRD patterns of KMn/Al_2O_3 samples. Diffraction peaks at 2θ = 29 ^{o}, 37 ^{o}, 43 ^{o}, 57^o and 59^o ascribed to crystalline β-MnO_2 (JCDS 24-0735) can be observed after supporting manganese oxides on alumina surfaces. When doping a small amount of potassium ions (K:Mn mole ratio less than 1:10) to the Mn/Al_2O_3 sample, the intensity of diffraction peaks assignable to crystalline β-MnO_2 greatly decreased, revealing that doping potassium promoted the dispersion of active Mn species with low crystallinity on the surface of the catalyst. Structure defects associated with the poor crystallinity led to the presence of oxygen vacancies in the KMn/Al_2O_3 sample [34]. The oxygen vacancies were generally recognized as adsorption-desorption centers for oxygen from the gaseous phases and

consequently acted as active sites in oxidation reactions [35]. When increasing the K:Mn mole ratio to 1:2, new diffraction peaks at $2\theta = 13^o$, 18^o, 50^o and 60^o assignable to crystalline α-MnO_2 (JCDS 44-0141) appeared, indicating that excessive amounts of potassium resulted in the formation of α-MnO_2. [ZJ(1]

The MnO_2-based materials are made up of MnO_6 octahedra, which join either corner -to-corner or edge-to-edge to form β-MnO_2 with (1x1) tunnel and α-MnO_2 with (2x2) tunnel, respectively [28]. In the (1x1) tunnel of β-MnO_2, the longest O-O bond length is only 3.175 Å, thus, it is not big enough to encompass a potassium atom. Our DFT calculations indicated that the addition of K atom leads to the large surface distortion and the surface Mn-O bond broken. Cockayne et al. studied K doping in bulk β-MnO_2 and had similar findings [28]. Apart from interstitial position, K atom is able to absorb on top of the surface. We considered two adsorption sites, including the top site (on top of O_{br}) and bridge site (in between of two O_{br}). We found that the surface adsorption of K atom is energetically more favorable than the interstitial adsorption. The total energy is lowered by at least 6.03 eV. Comparing the top site (E_{ad} = -4.53 eV) and the bridge site (E_{ad} = -4.75 eV), adsorption at the bridge site is more stable by 0.22 eV. Therefore, K atom would be initially adsorbed on the top of the β-MnO_2 surface rather than interstitial position. With the increase of the amount of potassium, the structure is gradually destroyed, leading to poor crystalline. When the phase transformation occurred, K is able to exist in the 2x2 tunnel of α-MnO_2. The computed adsorption energy is -5.67 eV and the distance in between of K and first neighbor O atoms ranges from 2.816 Å to 3.018 Å.

In order to understand the influence of K dopant and oxide structure on catalytic activity from theoretical point of view, we investigated O_2 and CO adsorption behaviors as well as CO oxidation reactions on β-MnO_2 (110) and α-MnO_2 (100) surfaces. The results are summarized in Table 4 and Table 5. We found that CO binds to the perfect stoichiometric

β-MnO_2 (110) surface via Mn_{5c} site (as shown in Figure 5) with the adsorption energy of -0.14 eV. However, O_2 molecule has a very weak interaction with the perfect surface. The adsorption energy is only -0.04 eV, which is similar to the value of -0.07 eV reported in the recent DFT study [27]. Therefore, on the stoichiometric β-MnO_2 (110) surface CO will be initially oxidized by the lattice O_{br} to form CO_2 and leave an O vacancy behind. It is an exothermic process with the energy barrier of 0.13 eV and the reaction energy ($E_r = E_{product} - E_{reactor}$) of -3.38 eV. Experimentally, the addition of K atom significantly changes the catalytic activity of the KMn/Al_2O_3 catalyst. According to our DFT calculations, K dopant weakens the interaction in between of CO and Mn_{5c} (E_{ad} is decreased to -0.05 eV), and facilitates the CO + O_{br} oxidation reaction on the β-MnO_2 (110) surface with the energy barrier of 0.09 eV. In addition, the K adsorption further activates O_2 bound at the O vacancy site. In the presence of K atom, the adsorption energy of O_2 is increased to -0.16 eV from -0.06 eV and the O-O bond length is elongated to 1.283 Å from 1.242 Å. The activation of the O_2 molecule is able to help generate a new lattice O to fill the vacancy site and sustain the catalytic cycle. Yang et al found that alkaline earth metal oxides promote CO oxidation over TiO_2-supported Au nanoparticles through electron transfer from alkaline metal to catalyst surface [19]. Similar charge redistribution is expected for the case of K-doped manganese oxides. Our bader charge calculation [39] indicated that the O_{br} atom on β-MnO_2 (110) surface has the charge of 6.68 |*e*|, which is very close to the value of 6.7 electrons in the literature [40]. However, the addition of potassium destroys the original charge balance on the surface. We found that K transfers 0.92 electrons to neighboring O atoms, and the bader charges on the nearest O_{br} atoms increase from 6.68 |*e*| to 6.90 |*e*|. The charge transfer leads to electron-rich MnO_2 surface and alters surface reactivity, which may enhance CO oxidation activity.

It is worth to note that a phase transformation in MnO_2 can be experimentally observed when increasing the amount of K dopant. It is generally accepted that the phase structure can significantly influence the catalytic activity of MnO_2 [36-38]. Indeed, accompanying with structure changes, the distortion of Mn octahedral coordination geometry modifies the orbital arrangement and energy, which definitely affects the adsorption behavior of reactants, and thus changes the catalytic performance. We studied the K-doped α-MnO_2 (100) surface and found that the adsorption of CO on α-MnO_2 (100) surface (E_{ad} = -0.23 eV) is stronger than that on the β-MnO_2 (110) surface with/without K adsorption (E_{ad} = -0.05 eV and -0.14 eV, respectively). Importantly, the calculated energy barriers of CO oxidation by lattice O_{br} is increased to 0.26 eV, compared to 0.09 eV on the K-adsorbed β-MnO_2 (110) surface. Thus, compared to the K-doped α-MnO_2 (100) surface, CO oxidation by lattice O is more facile on the K-adsorbed β-MnO_2 (110) surface. The computational results explain why a suitable amount of K doping enhances the catalytic performance, while excessive doping leads to a decline in catalytic activity.

Indeed, apart from surface morphology, K doping also modifies the surface atomic composition and manganese oxidation states, which are highly related with the catalytic activity. Thus, in this work, XPS was used to further examine these characteristics of the KMn/Al_2O_3 catalysts. As shown in Table 3, the surface Mn concentration varied by adding potassium ions. Doping a small amount of potassium ions (K:Mn mole ratio less than 1:10) to the Mn/Al_2O_3 sample greatly enriched the catalyst surface with Mn species. For K_1Mn_{10}/Al_2O_3 catalyst with the highest catalytic activity for CO oxidation, the Mn surface concentration was more than ca. 12.1%. An excess amount of potassium does not remarkably increase the Mn surface concentration. Although K_1Mn_2/Al_2O_3 also possessed a high Mn surface concentration, the catalytic activity was poor, implying the Mn surface concentration is not a determining factor to change the catalytic activity of KMn/Al_2O_3 catalyst.

The core-level spectra of Mn 2p and O 1s were presented in Figure 6. The spectrum of Mn 2p (Fig. 6(A)) displayed clear spin orbit splitting peaks, and the peaks at about 641.8 and 653.3 eV were assigned to Mn $2p_{3/2}$ and Mn $2p_{1/2}$ respectively [35, 41]. The very broad Mn $2p_{3/2}$ peak suggested the presence of multiple manganese species. The deconvolution of Mn $2p_{3/2}$ peak was known to be useful to distinguish different manganese species and the fitting results were given in Figure 6(A) and Table 6. The binding energies of Mn $2p_{3/2}$ in the intervals 639.8-640.3 eV, 641.5-641.7 eV and 643.2-643.5 eV were ascribed to the presence of Mn^{2+}, Mn^{3+} and Mn^{4+} ions, respectively [42, 43]. Adding a small amount of potassium ions (K:Mn mole ratio less than 1:10) remarkably decreased the population of Mn^{4+} and/or Mn^{3+} species, implying that Mn^{4+} and/or Mn^{3+} species were partially converted to Mn^{2+} species by doping potassium. The oxidation state of manganese oxide had a great impact on the surface oxygen species: a higher manganese state (Mn^{4+}) produced more surface adsorbed oxygen species, such as O^{2-}, and O^{-}, and a lower manganese state (Mn^{2+}) existing in the crystal generated oxygen vacancy which promoted the mobility of lattice oxygen [44]. The catalytic oxidation of CO on various manganese oxides has been extensively studied and suggested to follow a Mar-van Krevelen reaction mechanism [45-47]. According to this mechanism, the surface adsorbed CO reacts with a labile lattice oxygen to form CO_2 [45, 46]. Therefore, the excellent catalytic activity of K_1Mn_{10}/Al_2O_3 catalyst for CO oxidation can be attributed to the high oxygen mobility. With further addition of potassium to the Mn/Al_2O_3 sample, the concentration of Mn^{4+} species remained unchanged; the Mn^{2+} species were partially transformed to Mn^{3+} species and the decrease of catalytic activity appeared.

The O1s spectra of KMn/Al_2O_3 samples are shown in Figure 6(B). Three types of oxygen species can be identified. The low binding energy peaks at 529-530 eV were ascribed to the lattice oxygen (O^{2-}) (hereafter denoted as O_I); the medium binding energy peaks at 531-532 eV were related to surface adsorbed oxygen (O_2^- or O^-), OH groups and oxygen

vacancies (hereafter denoted as O_{II}); and the high binding energy peaks (above 533 eV) were likely to be associated with adsorbed molecular water (hereafter denoted as O_{III}) [48]. The relative abundances of O_I, O_{II} and O_{III} species are listed in Table 6. K_1Mn_{10}/Al_2O_3 sample with the highest catalytic activity possessed remarkably more lattice oxygen species (O_I). Additionally, the binding energy for O_I is the lowest for K_1Mn_{10}/Al_2O_3 sample, which can be associated to higher lattice oxygen mobility [49].

O_2-TPD technique has been proved to be useful to investigate the oxygen species of single and mixed oxides, throwing light on the type of oxygen species and their catalytic properties [50, 51]. Figure 7 showed the O_2-TPD profiles of the KMn/Al_2O_3 samples. The O_2-TPD pattern of Mn/Al_2O_3 was characterized by two major peaks at 520 and 785 ^oC. The first peak exhibited a small shoulder due to the desorption of surface oxygen species (O^- and O_2^-) or the presence of labile oxygen species with different Mn-O bond strengths. According to the literature [51, 52], the first peak was assigned to the transformation of β-MnO_2 to Mn_2O_3, and the second peak corresponded to the subsequent reduction of Mn_2O_3 to Mn_3O_4. Moreover, an additional peak at higher temperature, which may be caused by an intermediate transformation [51], was observed. A similar pattern was seen for the K_1Mn_{10}/Al_2O_3 sample, and the first peak slightly shifted to a lower temperature, showing lower stability. The difference in the stability between Mn/Al_2O_3 and K_1Mn_{10}/Al_2O_3 can be explained by the structural changes caused by the addition of potassium. The O_2-TPD profile of the K_1Mn_2/Al_2O_3 showed three peaks between 400 and 900 ^oC. A small peak at the temperature of 500 ^oC can be resulted from desorption of surface oxygen species (O^- and O_2^-) and /or the presence of labile oxygen species [53]. The major peak at 650 ^oC can be assigned to desorption of lattice oxygen species. According to XRD results, a transformation of supported α-MnO_2 to Mn_2O_3 might be occurred. The peak at the higher temperature is attributed to the transformation of Mn_2O_3 to Mn_3O_4. Compared to the Mn/Al_2O_3 and

K_1Mn_{10}/Al_2O_3, K_1Mn_2/Al_2O_3 sample showed higher stability (the peak assigned to lattice oxygen shifted to a higher temperature). Therefore, the structure changes caused by the doped potassium ions played an important role on the stability of lattice oxygen.

The reactivity of oxygen species of KMn/Al_2O_3 samples was also studied by H_2-TPR technique. As shown in Figure 8, the Mn/Al_2O_3 sample exhibited two major reduction peaks centered at 400 and 480 ^oC. The low-temperature peak could be assigned to the reduction of β-MnO_2 to Mn_3O_4, while the high-temperature reduction could be due to the reduction of Mn_3O_4 to MnO [51]. The H_2-TPR profile of the K_1Mn_{10}/Al_2O_3 sample was similar to that of the Mn/Al_2O_3 sample, but the low-temperature reduction peak shifted to a lower temperature, which was related to higher reducibility (thus, higher reactivity) in this particular sample [51]. Also the reduction peaks became broader, which is explained by higher heterogeneity of species [38]. The observed result was essentially consistent with XPS results, further confirming that Mn^{4+} and/or Mn^{3+} species were partially converted to Mn^{2+} species by doping potassium. A lower manganese oxidation state (Mn^{2+}) existing in the crystal generated oxygen vacancy that can increase the lattice oxygen mobility and thus enhanced the CO oxidation activity. The reduction pattern of K_1Mn_2/Al_2O_3 was different from the previous two samples, characterized by one small shoulder peak and two main reduction peaks at 371, 417 and 455 ^oC, respectively. The small shoulder at low temperature revealed the presence of labile species with different Mn-O strengths [51], which is in agreement with the O_2-TPD results. Those species were not strongly stabilized within the oxide lattice, and could be regarded as the surface reactive species [51]. According to XRD and O_2-TPD results, the main peak at 417 ^oC is associated with the reduction of α-MnO_2 to Mn_3O_4, whereas the high temperature peak at about 455 ^oC is assigned to the reduction of Mn_3O_4 to MnO. Compared to K_1Mn_{10}/Al_2O_3 sample, the main reduction peaks of K_1Mn_2/Al_2O_3 evidently shifted to a

higher temperature, implying that the redox activities of the catalyst was reduced by adding excessive amounts of potassium dopant.

Conclusions

In summary, the amount of K-dopant had a great influence on the structure and the catalytic activity of the KMn/Al_2O_3 catalyst.. Doping a small amount of potassium ions (K: Mn mole ratio less than 1:10) to Mn/Al_2O_3 catalyst induced the formation of β-MnO_2 phase with low crystallinity and enhanced the dispersion of active Mn species on the surface of the catalyst. In addition, the charge transfer from K to the catalyst surface probably increased the reducibility of Mn species and changed the reactivity of the lattice oxygen. We found that the K_1Mn_{10}/Al_2O_3 catalyst showed the best catalytic performance for the CO oxidation reaction, which effectively decreased the reaction temperature to 260 ℃. However, the more potassium dopants (K_1Mn_2/Al_2O_3) led to α-phase MnO_2 and higher reaction temperature. Further DFT calculations indicated that K doping activated O_2 adsorbed at the O vacancy site and made the CO oxidation easier, however, phase transformation strengthened reactant-catalyst interaction and increased CO-$O_{lattice}$ oxidation barrier to 0.26 eV. In this work, extensive experimental evidence plus DFT calculations may provide new insights to better understand and design KMn/Al_2O_3 catalyst for CO oxidation reaction.

Acknowledgments

This work was supported by scientific research key project fund of Department of Education of Henan Province (14A150043) and Program for Innovative Research Team in Science and Technology in University of Henan Province (15IRTSTHN003). Y. Yang acknowledges the financial support from the National Research Foundation (NRF), Prime Minister's Office, Singapore under its Campus for Research Excellence and Technological Enterprise (CREATE) program, AcRF Tier 1 grant (RG129/14), Ministry of Education,

Singapore, and Agency for Science, Technology and Research (A*STAR), Singapore. We also thankthe provision of computing facilities by the A*CRC (A*STAR Computing Resource Center).

References

[1] D. Gamarra, C. Belver, M. Fernández-García, A. Martínez-Arias, J. Am. Chem. Soc. 129 (2007) 12064-12065.

[2] B. K. Min, C. M. Friend, Chem. Rev. 107 (2007) 2709-2724.

[3] M. A. Bollinger, M. A. Vannice, Appl. Catal. B-Environ. 8 (1996) 417-443.

[4] A. Wolf, F. Schuth, Appl. Catal. A-Gen. 226 (1996) 1-13.

[5] D. R. Schryer, B. T. Upchurch, B. D. Sidney, K. G. Brown, G. B. Hoflund, R. K. Herz, J. Catal. 130 (1991) 314-317.

[6] G. Cahiez, M. Alami, R. J. K. Tayor, M. Reid, J. S. Foot, in: L.A. Paquette (Ed.), Encyclopedia of Reagents of Organic Synthesis, J. Wiley & Sons, New York, 2004.

[7] S. L. Suib, J. Mater. Chem. 18 (2008) 1623-1631.

[8] T. Oishi, K. Yamaguchi, N. Mizuno, ACS Catal. 1(2011)1351-1354.

[9] W. Y. Hernández, M. A. Centeno, S. Ivanova, P. Eloy, E. M. Gaigneaux, J. A. Odriozola, Appl. Catal. B- Environ. 123-124 (2012) 27-35.

[10] K. Qian, Z. Qian, Q. Hua, Z. Jiang, W. Huang, Appl. Surf. Sci. 273 (2013) 257-263.

[11]Y. Hasegawa, K. Fukumoto, T. Ishima, H. Yamamoto, M. Sano, T. Miyake, Appl. Catal. B-Environ. 89 (2009) 420-424.

[12] O. A. Bulavchenko, T. N. Afonasenko, P. G. Tsyrul'nikov, S. V. Tsybulya, Appl. Catal. A-Gen. 459 (2013) 473-80.

[13] N. Pasha, N. Lingaiah, P. S. S. Reddy, P. S. S. Prasad, Catal. Lett. 118 (2007) 64-68.

[14] Y. V. Larichev, B. L. Moroz, V. I. Zaikovskii, S. M. Yunusov, E. S. Kalyuzhnaya, V. B. Shur, V. I. Bukhtiyarov, J. Phys. Chem. C 111 (2007) 9427-9436.

[15] Q. H. Zhang, Q. Guo, X. X. Wang, T. Shishido, Y. Wang, J. Catal. 239 (2006) 105-116.

[16] B. Mirkelamoglu, G. Karakas, Appl. Catal. A-Gen. 299 (2006) 84-94.

[17] C. Wang, G. Yi, H. Lin, Y. Yuan, Inter. J. Hydrogen energy 37 (2012) 14124-14132.

[18] Y. Zhang, S. Wu, L. Jin, D. Xie, Inter. J. Hydrogen energy 39 (2014) 118668-18674.

[19] K. Yang, Y. Zhang, Y. Li, P. Huang, X. Chen, W. Dai, X. Fu, Appl. Catal. B- Environ. 183 (2016) 206-215.

[20] Q. H. Tang, T. Liu, Y. H. Yang, Catal. Commun. 9 (2008) 2570-2573.

[21] G. Kresse, J. Hafner, Phys. Rev. B 48 (1993) 13115-13126.

[22] G Kresse, J. Hafner, Phys. Rev. B 49 (1994) 14251-14269.

[23] P. E. Bloechl, Phys. Rev. B 50 (1994) 17953-17979.

[24] G. Kresse, D. Joubert, Phys. Rev. B 59 (1999) 1758-1775.

[25] J.P. Perdew, K. Burke, M. Ernzerhof, Phys. Rev. Lett.77 (1996) 3865-3868.

[26] S. L. Dudarev, G. A. Botton, S. Y. Savrasov, C .J. Humphreys, A. P. Sutton, Phys. Rev. B 57 (1998) 1505-1509.

[27] F. Cheng, T. Zhang, Y. Zhang, J. Du, X. Han, J. Chen, Angew. Chem. Int. Ed. 52 (2013) 2474-2477.

[28] E. Cockayne, L. Li, Chem. Phys. Lett. 544 (2012) 53-58.

[29] C. S. Johnson, D. W. Dees, M. F. Mansuetto, M. M. Thackeray, D .R. Vissers, D. Argyriou, C. K. Loong, L. Christensen, J. Power Sources 68 (1997) 570-577.

[30] W. Baur, Acta Crystallagr. B 32 (1976) 2200-2206.

[31] D.A. Tompsett, S. C. Parker, M. S. Islam, J. Mater. Chem. A 2 (2014) 15509-15518.

[32] D. A. Tompsett, S. C. Parker, M. S. Islam, J. Am. Chem. Soc. 136 (2014) 1418-1426.

[33] A. Alavi, P. Hu, T. Deutsch, P. L. Silvestrelli, J. Hutterm, Phys. Rev. Lett. 80 (1998) 3650-3653.

[34] M. R. Morales, B. P. Barbero, L. E. Cadús, Fuel 87 (2008) 1177-1186.

[35] M. R. Morales, F. N. Agüero, L. E. Cadús, Catal. Lett. 143 (2013) 1003-1011.

[36] R. Xu, X. Wang, D. Wang, K. Zhou, Y. Li, J. Catal. 237 (2006) 426-430.

[37] S. Liang, F. Teng, G. Bulgan, R. Zong, Y. Zhu, J. Phys. Chem. C 112 (2008) 5307-5315.

[38] Z. Qu, Y. Bu, Y. Qin, Y. Wang, Q. Fu, Chem. Eng. J 209 (2012) 163-169.

[39] G. Henkelman, A. Arnaldsson, H. Jónsson, Comput. Mater. Sci. 36 (2006) 254-360.

[40] D. A. Tompsett, M. Saiful Islam J. Phys. Chem. C 118 (2014) 25009-25015.

[41] M. Kang, E. D. Park, J. M. Kim, J. E. Yie, Appl. Catal. A-Gen. 327 (2007) 261-269.

[42] X. Lou, P. Liu, J. Li, Z. Li, K. He, Appl. Surf. Sci. 307 (2014) 382-387.

[43] Y. Dai, X. Y. Wang, Q. G. Dai, D. Li, Appl. Catal. B-Environ. 111-112 (2012) 141-146.

[44] W. Tang, X. Wu, D. Li, Z. Wang, G. Liu, H. Liu, Y. Chen, J. Mater. Chem. A 2 (2014) 2544-2554.

[45] K. Ramesh, L. Chen, F. Chen, Y. Liu, Z. Wang, Y. Han, Catal. Today 131 (2008) 477-482.

[46] M. Ozacar, A. S. Poyraz, H. C. Genuino, C. Hou, Y. Meng, S. L. Suib, Appl. Catal. A-Gen. 462-463 (2013) 64-74.

[47] A. S. Poyraz, W. Song, D. Kriz, C.-H. Kuo, M. S. Seraji, S. L. Suib, Appl. Mater. Interfaces 6 (2014) 10986-10991.

[48] T. Garcia, D. Sellick, F. Varela, I. Vázquez, A. Dejoz, S Agouram, S. H. Taylor, B. Solsona, Appl. Catal. A-Gen. 450 (2013) 169-177.

[49] E. C. Njagi, C. -H. Chen, H. Genuino, H. Galindo, H. Huang, S. L. Suib, Appl. Catal. B-Environ. 99 (2010) 103-110.

[50] B. Levasseur, S. Kaliagunine, Appl. Catal. B-Environ. 88 (2009) 305-314.

[51] V. P. Santos, M. F. R. Pereira, J. J. M. Orfao, J. L. Figueiredo, Appl. Catal. B-Environ. 99 (2010) 353-363

[52] J. Luo, Q. Zhang, J. Garcia-Martinez, S. L. Suib, J. Am. Chem. Soc. 130 (2008)

3198-3207.

[53] O. A. Bulavchenko, T. N. Afonasenko, P. G. Tsyrul’nikov, S. V. Tsybulya, Appl. Catal. A-Gen. 459 (2013) 73-80.

Figure captions

Figure 1 Side view and top view of partially optimized MnO_2 surfaces: (a) and (b) for β-MnO_2 (110) surface; (c) and (d) for α-MnO_2 (100) surface. All surface Mn and O are labelled. In (b) and (d) (top view of the surface slabs), remove O_{br} to create an O vacancy.

Figure 2 The comparison of CO oxidation activity over different alkali metal-doped Mn catalysts.

Figure 3 The TOFs of CO oxidation over Mn/Al_2O_3, K_1Mn_{10}/Al_2O_3 and K_1Mn_2/Al_2O_3 catalysts.

Figure 4 XRD patterns of (a) γ-Al_2O_3, Symbols of ♦, ∗, • and + denote α-MnO_2, β-MnO_2, AlO(OH) and Al_2O_3.

Figure 5 Optimized structures of (a) CO adsorbed at the Mn_{5c} site on the β-MnO_2 (110) surface, which is the initial state of the CO oxidation by lattice O_{br}; (b) transition state (TS) of the CO oxidation by lattice O_{br} on β-MnO_2 (110); (c) CO_2 on the β-MnO_2 (110) surface with O vacancy, which is the final state of the CO oxidation by lattice O_{br}; (d) TS of the CO oxidation by lattice O_{br} on K-adsorbed β-MnO_2 (110); (e) TS of the CO oxidation by lattice O_{br} on K-doped α-MnO_2 (100) surface. The atoms associated with the C-O bond formation are highlighted.

Figure 6(A) Mn 2p and (B) O 1s XPS of (a) Mn/Al_2O_3, (b) K_1Mn_{10}/Al_2O_3, (c) K_1Mn_2/Al_2O_3.

Figure 7 O_2-TPD patterns of (a) Mn/Al_2O_3, (b) K_1Mn_{10}/Al_2O_3, (c) K_1Mn_2/Al_2O_3.

Figure 8 H_2-TPR patterns of (a) Mn/Al_2O_3, (b) K_1Mn_{10}/Al_2O_3, (c) K_1Mn_2/Al_2O_3.

Table 1. Calculated and experimental lattice parameters of bulk α-MnO_2 and β-MnO_2.

Bulk		a=b (Å)	c (Å)
α-MnO_2	Calculated	9.729	2.894
	Experimental[26]	9.750	2.861
β-MnO_2	Calculated	4.417	2.905
	Experimental[27]	4.398	2.873

Table 2. Relative energies to remove a lattice O from α-MnO_2 (100) surface and β-MnO_2 (110) surface, respectively.

Surface	Site	Relative Energy (eV)
α-MnO_2 (100)	O_{br}	-2.10
	O_{IP1}	-1.15
	O_{IP2} (reference)	0
	O_{IP3}	-0.40
β-MnO_2 (110)	O_{br}	-1.51
	O_{IP} (reference)	0

Table 3. List of catalysts prepared.

Entry	Catalyst	Me:Mn[a]	Mn loading[b] (wt%)	SA[c] (m^2/g)	Atomic percentage (%)[d]			
					Al 2p	O 1s	K 2p	Mn 2p
1	Al_2O_3	-	-	193	-	-	-	-
2	Mn/Al_2O_3	-	9.83	169	14.0	77.3	0.0	8.7
3	K_1Mn_{10}/Al_2O_3	1:10	9.76	178	8.4	79.2	0.3	12.1
4	K_1Mn_2/Al_2O_3	1:2	9.65	167	9.0	71.2	3.4	16.4
5	Li_1Mn_{10}/Al_2O_3	1:10	9.75	162	-	-	-	-
6	Na_1Mn_{10}/Al_2O_3	1:10	9.81	158	-	-	-	-
7	Mg_1Mn_{10}/Al_2O_3	1:10	9.68	159	-	-	-	-
8	Ca_1Mn_{10}/Al_2O_3	1:10	9.73	161	-	-	-	-

[a] Molar ratio of Me to Mn (Me = Li, Na, K, Mg ,Ca).

[b] The Mn loading in each sample was determined by ICP-MS.

[c] Surface area by BET method.

[d] Surface atomic concentration determined from XPS.

Table 4. Adsorption energies (E_{ad}) and geometry parameters of reactants as well as K atom on α-MnO_2 (100) and β-MnO_2 (110) surfaces.

Surface	Adsorbate	E_{ad} (eV)	Adsorption Site	Adsorbate-surface distance (Å)	
α-MnO_2 (100)	K	-5.67	Within the 2x2 tunnel	K-O	2.816-3.018
K-doped α-MnO_2 (100)	CO	-0.23	Mn_{5c}	C-Mn_{5c}	2.238
	O_2	-0.05	Mn_{5c}	O-Mn_{5c}	2.972
				O-O	1.233
β-MnO_2 (110)	K	-4.75	Bridge site in between of two O_{br}	K-O_{br}	2.549/2.549
	CO	-0.14	Mn_{5c}	C-Mn_{5c}	2.377
	O_2	-0.04	Mn_{5c}	O-Mn_{5c}	2.946
				O-O	1.233
	O_2	-0.06	O_{br}vacancy	O-Mn_{6c}	2.570/2.497
				O-O	1.242
K-adsorbed β-MnO_2 (110)	CO	-0.05	Mn_{5c}	C-Mn_{5c}	2.414
	O_2	-0.16	O_{br} vacancy	O-Mn_{6c}	2.077/2.111
				O-O	1.283

Table 5. Energy barriers (E_a) and geometry parameters of transition states for CO oxidation by lattice O_{br}.

Surface	E_a (eV)	d_{Obr-C} (Å)	d_{Obr-Mn} (Å)	d_{C-Mn} (Å)
β-MnO_2 (110)	0.13	2.240	1.910/1.913	2.192
K-adsorbed β-MnO_2(110)	0.09	2.340	1.906/1.908	2.209
K-doped α-MnO_2 (100)	0.26	2.152	1.921/1.906	2.228

Table 6. XPS results of the KMn/Al_2O_3 catalysts.

Entry	Catalyst	Mn 2p3/2						O 1s					
		Mn^{2+}		Mn^{3+}		Mn^{4+}		O_I		O_{II}		O_{III}	
		BE (eV)	Area (%)	BE (eV)	Area (%)	BE (eV)	Area (%)	BE (eV)	Area (%)	BE (eV)	Area (%)	BE (eV)	Area (%)
1	Mn/Al_2O_3	-	-	641.6	70.2	643.5	29.8	529.0	8.4	531.1	81.8	533.0	9.8
2	K_1Mn_{10}/Al_2O_3	639.7	21.4	641.7	53.2	643.4	25.4	528.9	39.4	531.2	55.6	533.0	5.0
3	K_1Mn_2/Al_2O_3	640.3	16.2	641.5	58.8	643.2	25.0	529.3	21.1	531.0	67.5	533.0	11.4

O_I :MnO_x lattice oxygen (O^{2-}) ;

O_{II} : surface adsorbed oxygen (O_2^-or O^-), HO^-groups and oxygen vacancies;

O_{III}:adsorbed molecular water.

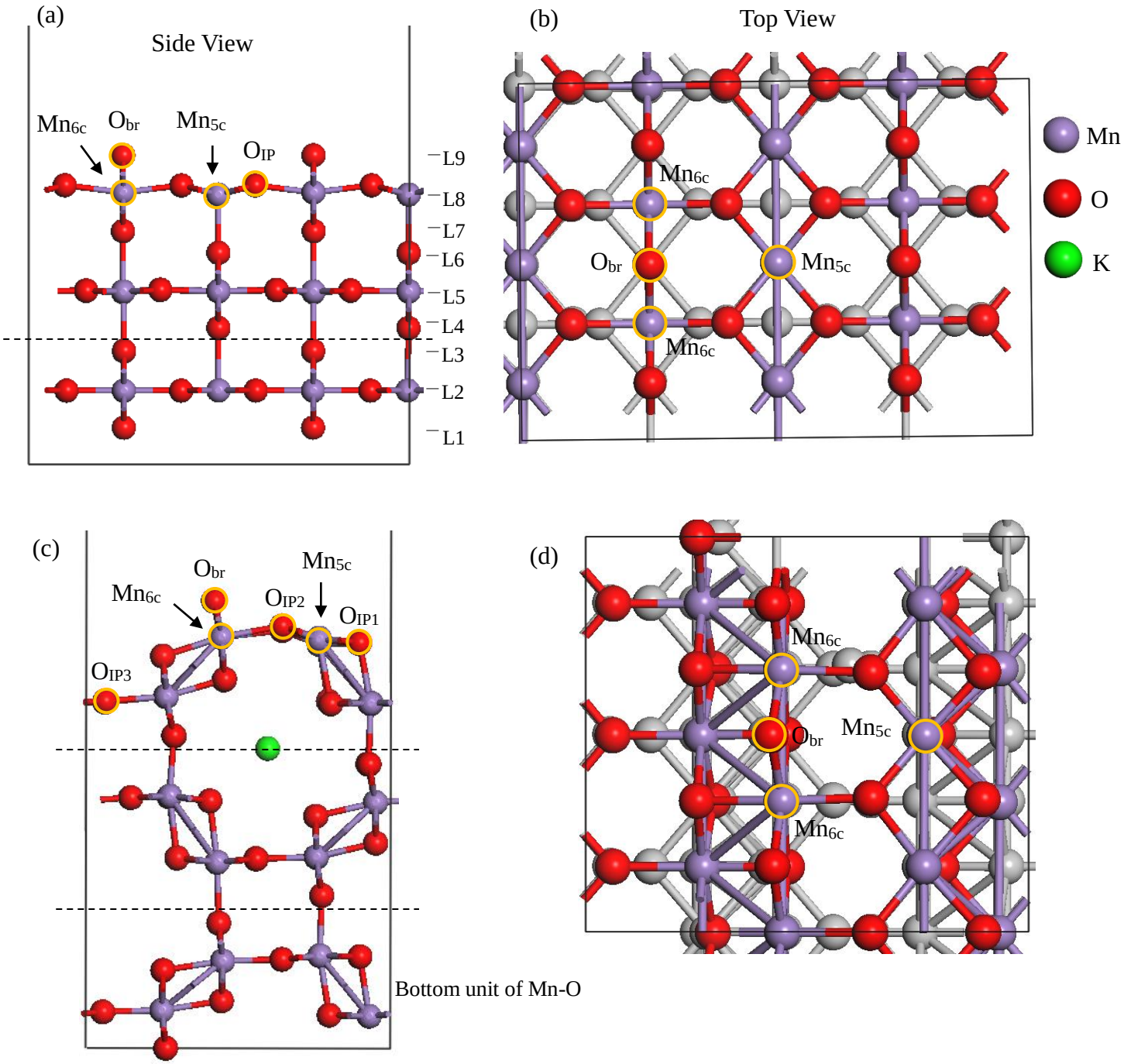

Bottom unit of Mn-O

Figure 1

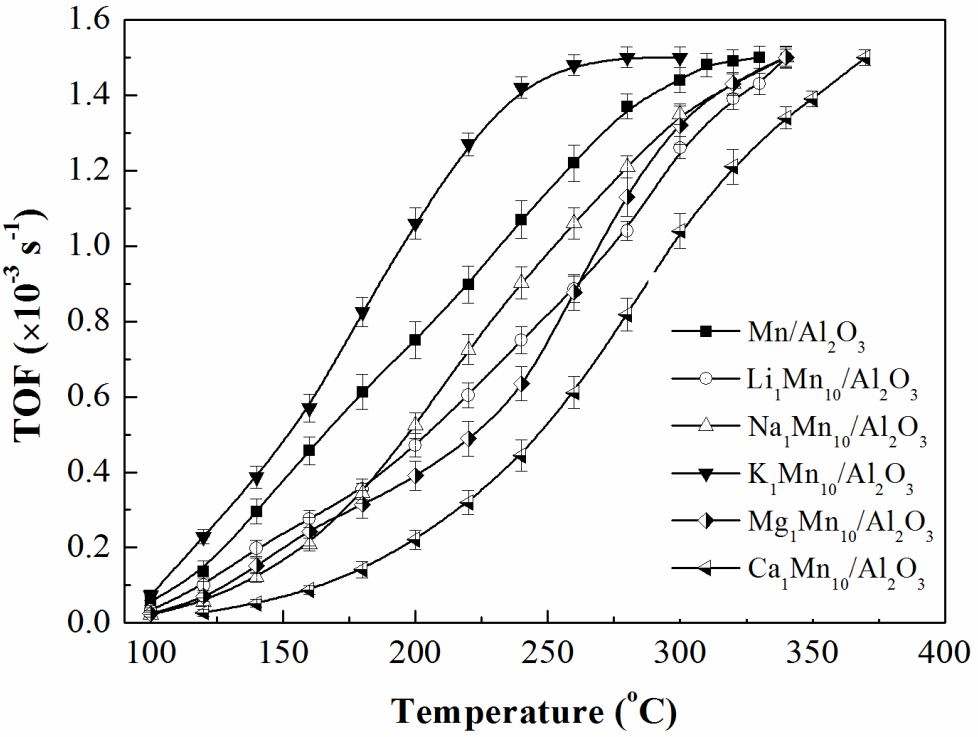
TOF (×10-3 s-1)
Temperature (°C)
Mn/Al2O3
Li1Mn10/Al2O3
Na1Mn10/Al2O3
K1Mn10/Al2O3
Mg1Mn10/Al2O3
Ca1Mn10/Al2O3

Figure 2

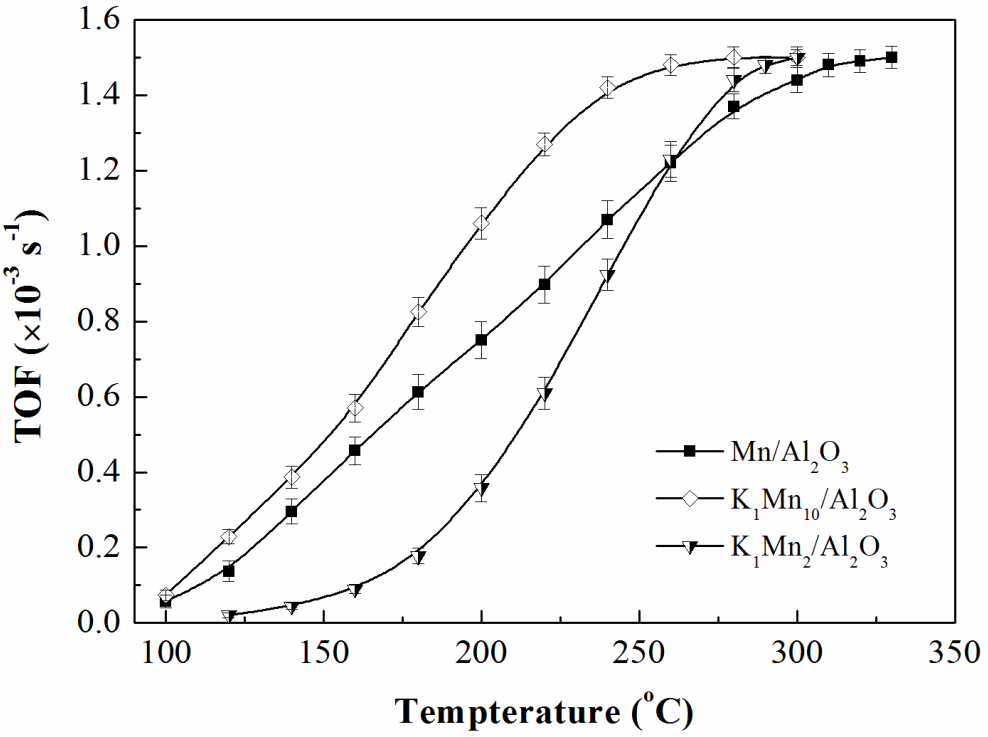
TOF (×10^{-3} s^{-1})
Tempterature (^{o}C)
Mn/Al$_2$O$_3$
K$_1$Mn$_{10}$/Al$_2$O$_3$
K$_1$Mn$_2$/Al$_2$O$_3$

Figure 3

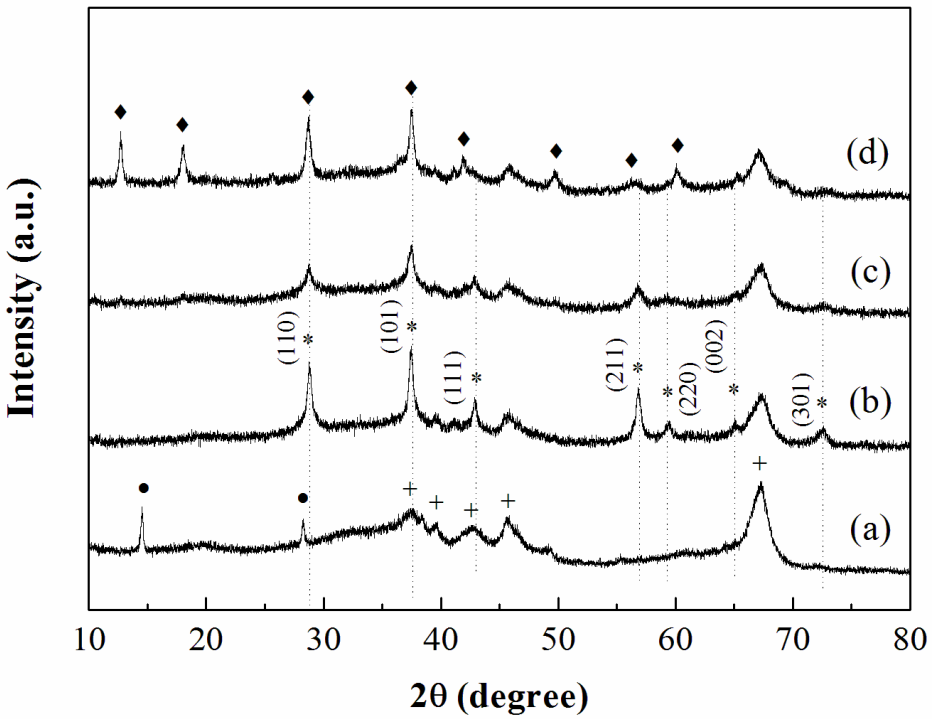
Intensity (a.u.)
2θ (degree)
10
20
30
40
50
60
70
80
(d)
(c)
(b)
(a)
(110)
(101)
(111)
(211)
(220)
(002)
(301)

Figure 4

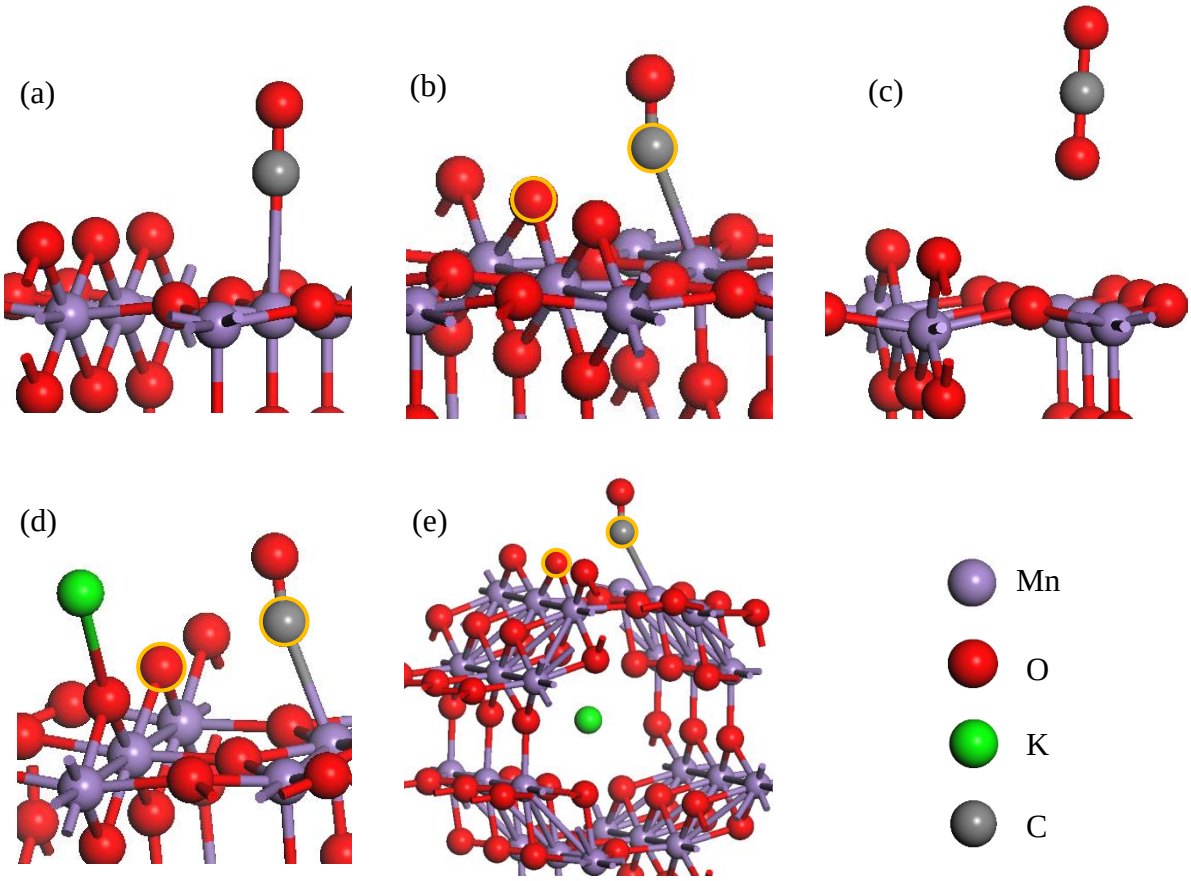

Figure 5

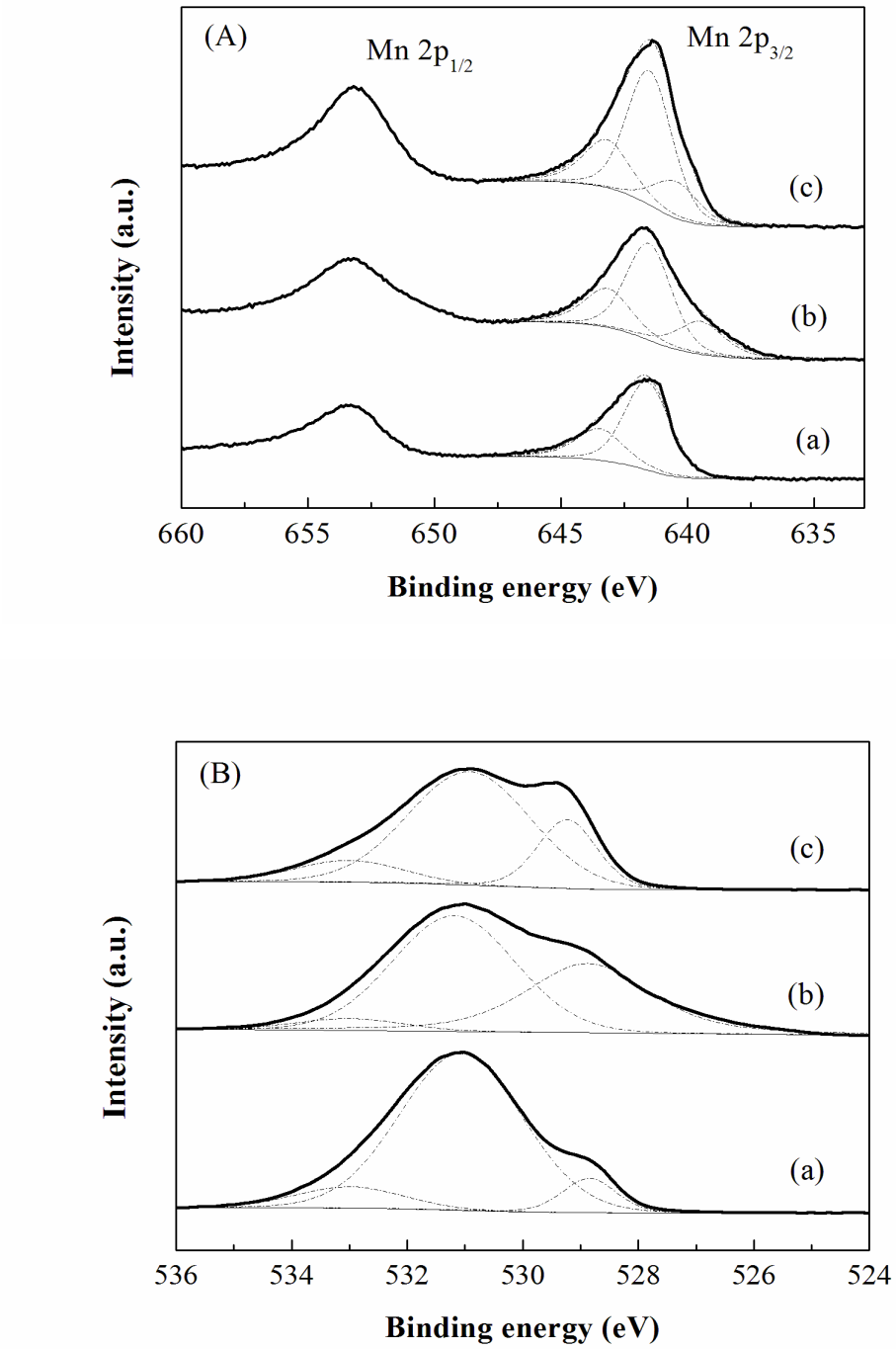
(A)
Mn 2p1/2
Mn 2p3/2
(c)
(b)
(a)
Intensity (a.u.)
660
655
650
645
640
635
Binding energy (eV)
(B)
(c)
(b)
(a)
Intensity (a.u.)
536
534
532
530
528
526
524
Binding energy (eV)

Figure 6

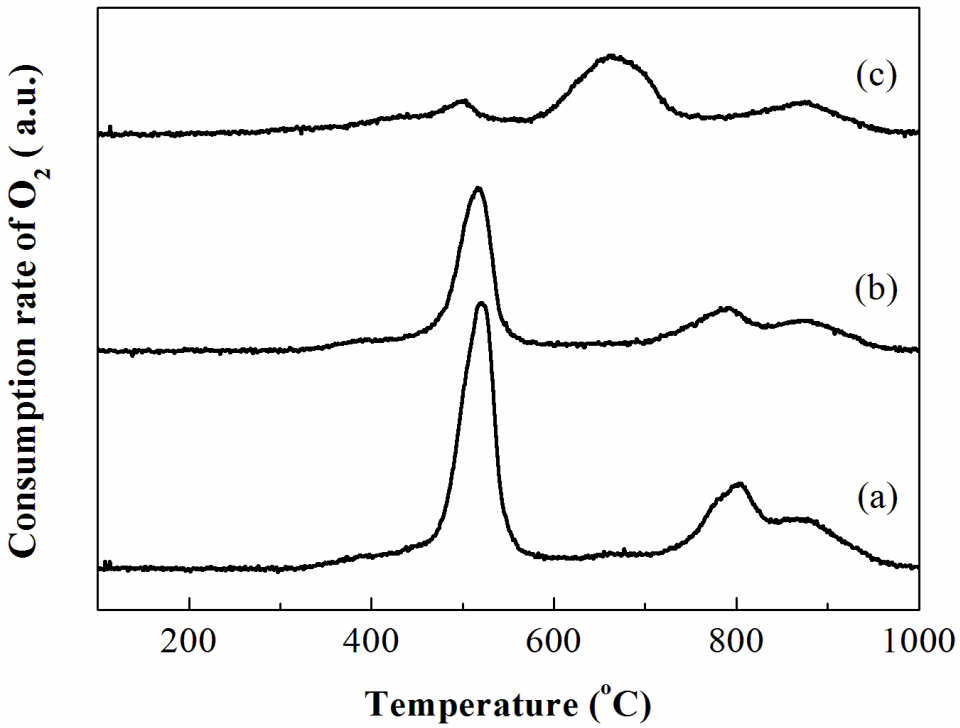
Consumption rate of O_2 (a.u.)
(c)
(b)
(a)
200
400
600
800
1000
Temperature (^{o}C)

Figure 7

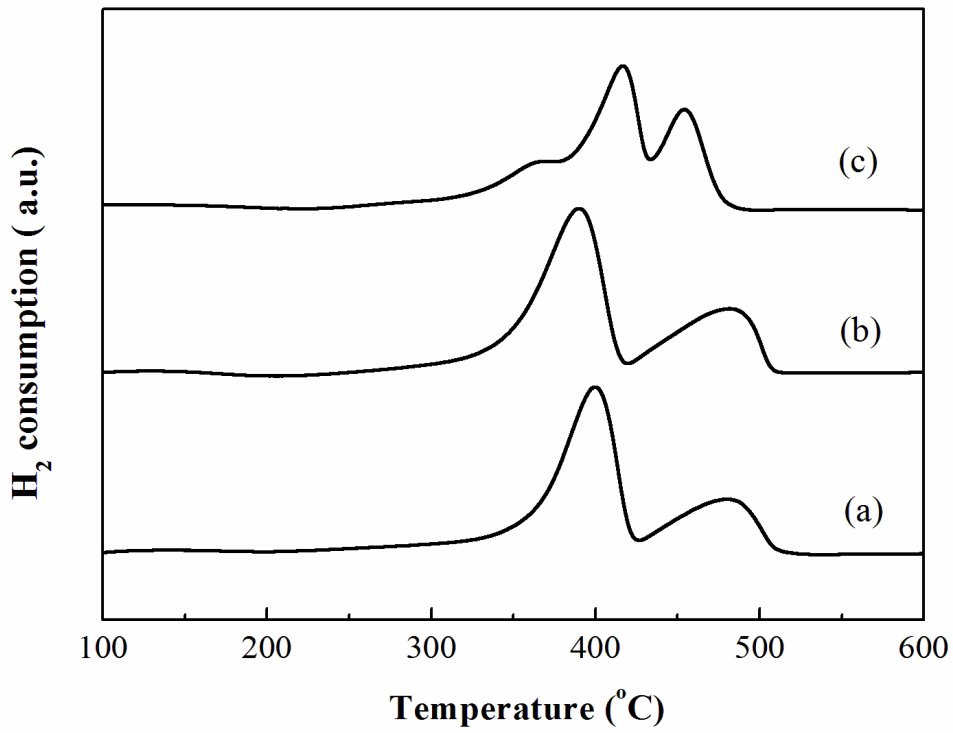

Figure 8